Ultrasonics 142 (2024) 107399

Contents lists available at ScienceDirect

Ultrasonics

journal homepage: www.elsevier.com/locate/ultras

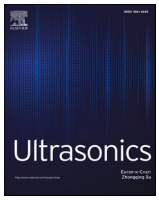

# Mode conversion of fundamental guided ultrasonic wave modes at part-thickness crack-like defects

Lijian Li *, Paul Fromme

*Department of Mechanical Engineering, University College London (UCL), London, UK*

ARTICLE INFO

*Keywords:*
Lamb waves
Scattering
Mode conversion
Guided waves
FE simulation
Experimental validation

ABSTRACT

Guided ultrasonic waves can be employed for efficient structural health monitoring (SHM) and non-destructive evaluation (NDE), as they can propagate long distances along thin structures. The scattering ($S_0$ mode) and mode conversion of low frequency guided waves ($S_0$ to $A_0$ and $SH_0$ wave modes) at part-thickness crack-like defects was studied to quantify the defect detection sensitivity. Three-dimensional (3D) Finite Element (FE) modelling was used to predict the mode conversion and scattering of the fundamental guided wave modes. Experimentally, the $S_0$ mode was excited by a piezoelectric (PZT) transducer in an aluminum plate. A laser vibrometer was used to measure the out-of-plane displacement to characterize the mode-converted $A_0$ mode, employing baseline subtraction to achieve mode and pulse separation. Good agreement between FE model predictions and experimental results was obtained for perpendicular incidence of the $S_0$ mode. The influence of defect depth and length on the scattering and mode conversion was studied and the sensitivity for part-thickness defects was quantified. The maximum mode conversion ($S_0$-$A_0$ mode) occurred for ¾ defect depth and the amplitude of the mode-converted $A_0$ and scattered $S_0$ modes mostly increased linearly as the defect length increased with an almost constant $A_0/S_0$ mode scattered amplitude ratio. Similar forward and backward scattering amplitude was found for the mode converted $A_0$ mode. The mode conversion of the $S_0$ to $SH_0$ mode has the highest sensitivity for short defects, but the $SH_0$ mode amplitude only increased slightly for longer defects. Employing the information contained in the mode-converted, scattered guided ultrasonic wave modes could improve the detection sensitivity and localization accuracy of SHM algorithms.

## 1. Introduction

Fatigue cracks cause 60 % of the total service failures in aircraft components [1]. Fatigue cracks initially generate at the microscopic level and then rapidly grow to a critical crack size causing fracture [2], potentially leading to serious consequences. To ensure aircraft safety, it is necessary to detect small, part-thickness fatigue cracks at an early stage [3], as fatigue crack growth increases exponentially under cyclic loading [2]. Depending on the application, cracks should be detected before they grow through the thickness of the structure to avoid leaks or significantly reduce its remaining strength [4]. Guided ultrasonic waves can provide efficient structural health monitoring (SHM) and non-destructive evaluation (NDE), as they can propagate long distances along thin, large structures with limited attenuation [5]. Lamb waves are elastic waves propagating in isotropic plate structures [6], where also shear horizontal (SH) waves exist, with the fundamental $SH_0$ mode having no dispersion. The fundamental symmetric ($S_0$) and anti-symmetric ($A_0$) Lamb wave modes below the cut-off frequencies of higher wave modes were widely used for NDE and SHM investigations [7–10]. At low frequency-thickness product, the dominant displacement of the $A_0$ wave mode is out-of-plane, while for the $S_0$ and $SH_0$ wave mode the in-plane displacement is dominant.

For SHM using guided waves, distributed sensors have been widely used to detect and localize defects in plate structures [7]. Low frequency Lamb waves (selective excitation of $A_0$ or $S_0$ mode below cut-off frequency of higher Lamb modes) were used to detect cracks in a plate using PZTs as sensors and actuators [8–10]. The long-term stability [11] and the influence of temperature change [12] and surface wetting [13] on detection sensitivity using baseline subtraction were investigated. To minimize the limitations of the baseline subtraction method, modifications were developed to improve detection results such as image fusion [14] and in-situ arrays of sensors [15], and the scattering patterns at defects were studied.

It is necessary to understand the scattering of guided waves at defects

* Corresponding author.
*E-mail address:* lijian.li.19@ucl.ac.uk (L. Li).

https://doi.org/10.1016/j.ultras.2024.107399
Received 20 February 2024; Received in revised form 2 July 2024; Accepted 3 July 2024
Available online 5 July 2024

and the influence of different parameters (e.g., defect size and excitation frequency) on detection results for the development of NDE and SHM methods [16]. The scattering of the $S_0$ [17], $A_0$ [18], and $SH_0$ [19] modes at part-thickness notches was investigated from 2D geometry FE simulations (assumed perpendicular incidence on infinite length defect) and validated from experiments in a steel plate with good agreement. A shallow crack (e.g., 31 % thickness) showed a lower sensitivity than a deep crack-like defect (75 % thickness) for the $A_0$ and $S_0$ wave modes. FE simulations were used to predict the mode converted $S_0$-$A_0$ wave pulses for a 2D plate model [20]. The $S_0$ mode interaction with through-thickness crack-like defects was investigated for varying lengths from 3D FE simulations with experimental validation [21]. The sensitivity was found to be frequency independent and increased as the defect length increased. For long cracks, oscillations occurred in the reflection coefficient curves due to the wave diffraction at the crack tip and interaction of waves along the crack surfaces. Compared with the $A_0$ mode, limited sensitivity of the $S_0$ mode for short defects was observed, as the $S_0$ mode has a long wavelength [21]. The scattering of guided ultrasonic waves at cracks in an aluminum plate structure was studied [16,22]. The influence of defect depth [16], length [16,22], and incident wave direction [16] on the scattered $A_0$ mode detection results were studied and quantified. Good agreement was obtained between experimental results and Finite Element (FE) simulations. The $SH_0$ wave mode scattering at a through-thickness [23,24] and part-thickness [25] notch in a thin aluminum plate was studied. For through-thickness notches, the detection sensitivity (amplitude) linearly increased as the center frequency or the defect length increased. For part-thickness notches, higher sensitivity was found for a deeper defect. The $A_0$ mode was used for defect detection of a defect (notch) at a through-thickness hole [26]. The influence of the excitation frequency on the scattering patterns was small for 0° incident wave angle (perpendicular to notch), and the scattering patterns were very similar as the hole diameter changed [27]. The baseline subtraction method was used to detect defects from rivet holes and a distortion of the scattering patterns was shown due to the cracks [28]. The detection of defects in the vicinity of five fastener holes and inside a lap joint by guided waves ($S_0$ wave mode) was studied [29]. Good agreement between FE and experimental results was obtained and a fatigue crack was successfully located.

Mode conversion is the phenomenon where part of the energy is transferred from one guided wave mode to other guided wave modes during interaction with defects [30]. For higher frequency-thickness products with multiple guided wave modes present, the mode conversion and scattering can be quite complex [31]. Below the cut-off frequencies of the higher guided wave modes in isotropic plates, mode conversion between the $S_0$ and $SH_0$ mode can occur for through-thickness defects [32]. Mode conversion between the $S_0$ and $A_0$ Lamb modes only occurs for non-symmetric defects (e.g., part-thickness fatigue crack growing from one plate surface) [33], due to the respectively symmetric and anti-symmetric mode shapes through the thickness.

SHM methodologies employing mode conversion have been developed to localize damage and estimate defect size. Guided wave mode conversion ($S_0$ mode to $A_0$ mode) was used for the localization of a crack-like defect in a plate from FE simulations [34]. The detection of the defect location was successful, employing time reversal of the mode-converted $A_0$ mode. A SHM methodology based on mode conversion ($A_0$ mode to $S_0$ mode) was developed employing 3D laser vibrometry [35]. Part-thickness cracks were detected, but not localized, from the mode conversion of Lamb waves ($A_0$ and $S_0$ modes) using a baseline-free methodology [36]. The energy difference caused by the mode conversion at defects was used to indicate whether a crack existed (or not), with both FE simulations and experiments conducted. The distance of a defect from the sensor and the notch depth and width were predicted from an analysis of the mode conversion ($S_0$-$A_0$ mode), based on theoretical calculations and FE simulations [37]. The localization process was based on the time difference between scattered modes at the receiver, and the scattering coefficients of the Lamb wave modes were used to predict the defect geometry. Defects could be localized experimentally in a plate using baseline-free mode conversion ($S_0$-$A_0$), employing two transducers [38]. The relation between the wave propagation velocities and distances was utilized to localize the defects. A deeper, half-thickness notch was localized successfully, but the method did not work for a shallow (1/10 thickness) notch. Transmission analysis with 2D-Fast Fourier Transform (FFT) of the mode conversion ($A_0$ and $S_0$ modes) at part-thickness defects was investigated [39]. The apparent group velocity of the mode-converted waves was used to localize the defect and separate the original transmitted modes ($A_0$-$A_0$, $S_0$-$S_0$) and mode converted waves. Guided wave mode conversion ($S_0$ mode to $A_0$ mode) at part-thickness holes was studied and the scattering for different frequencies and hole diameters was investigated [40]. From FE simulations, the scattering and mode conversion of an incident $S_0$ Lamb wave mode to the $A_0$ and $SH_0$ modes was studied for different depth and length of a part-thickness crack using a 3D plate model with absorbing boundary conditions [41]. It was found that the defect depth influenced the distribution of the energy transferred to the wave modes. For a 1/3 deep and 26.6 mm long crack (equivalent to $S_0$ mode wavelength), the mode converted scattered $A_0$ mode had the highest amplitude and the $S_0$ mode had the lowest amplitude, while for a through-thickness crack, the $SH_0$ mode had the highest amplitude. The influence of the defect length on the scattered mode patterns was investigated from scattering matrices.

Although the mode conversion between the fundamental guided wave modes has been investigated for part-thickness holes [35,40], cracks [36] and notches [34,38,39] in a plate, previous research on the mode-conversion of guided waves at part-thickness crack-like defects focused on FE simulations [20,41] and lacked experimental validation. Good agreement was previously obtained for scattered single guided wave modes ($A_0$ and $S_0$) at crack-like defects between FE simulations and experimental validation [16,21,22]. In this study, experimental validation of FE simulations for the $S_0$-$A_0$ mode conversion at crack-like defects was conducted. Based on this validation, the effects of multiple parameters and different defect geometries (length, depth) on the scattering ($S_0$ mode) and mode conversion ($A_0$, $SH_0$ modes) at part-thickness defects were investigated. The understanding and validation of 3D FE simulations of the scattered and mode-converted guided waves at part-thickness crack-like defects could be employed to improve previously proposed SHM and NDE methodologies for the detection of fatigue cracks at an early stage before growing through the structure thickness. FE simulations and experiments with varying defect depth and length were conducted to investigate guided wave scattering and mode conversion from the $S_0$ to the $A_0$ mode. The scattered $S_0$ and mode converted $SH_0$ modes were also quantified from the FE simulations to analyze the respective energy transfer. The experimental procedure and FE simulation settings are described and the results for mode conversion from $S_0$ to $A_0$ mode are compared with a good agreement. The influence of defect length and depth on the guided wave scattering is discussed.

## 2. Experiments

### 2.1. Experimental setup

A 1 mm wide, flat bottom notch was milled in steps as a single defect with increasing depth and length at the center of an aluminum plate (Al 6082, 1 m × 1 m × 5 mm, Fig. 1). Initially, a notch of length 20 mm and depth 1.25 mm (1/4 thickness) was milled in the workshop. The depth was then increased to a depth of 2.5 mm (1/2 thickness) and 3.75 mm (3/4 thickness). For the 3.75 mm deep notch the length was increased in three steps to 30 mm, 40 mm, and 50 mm (Table 1). Before introducing the initial defect, a baseline measurement (as detailed below) was conducted for the undamaged plate to quantify the incident wave field. After each milling step to increase the size of the single defect located at the plate center, the plate was transferred from the workshop to the laboratory to measure the scattering at the defect. The plate had to be re-

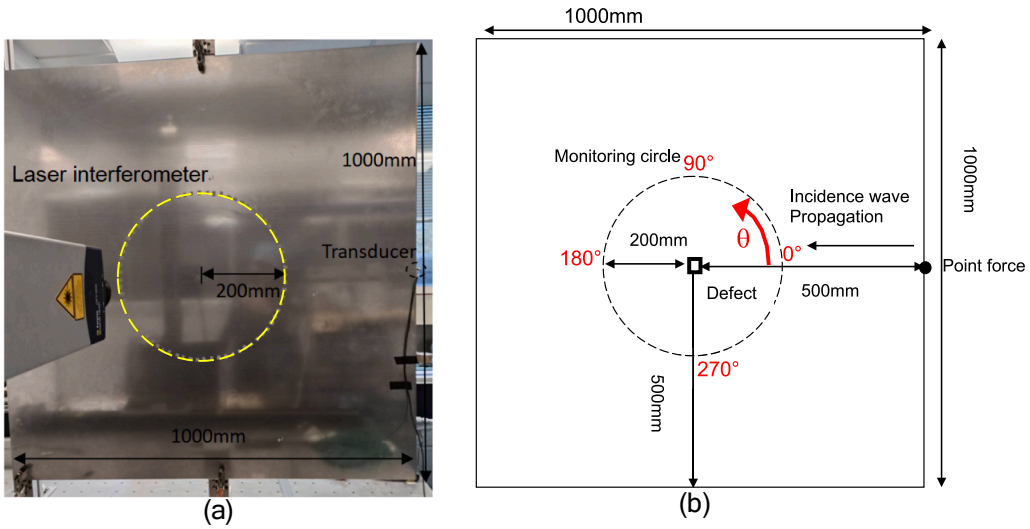


**Fig. 1.** (a) Photograph of experimental setup; (b) FE model. Aluminum plate (size: 1 m × 1 m × 5 mm) with 50 mm notch, excitation transducer (right plate edge), 200 mm radius monitoring circle for laser interferometer and FE output requests.

**Table 1**
Part-thickness notch size for each milling step and measurement.

| Notch length (mm) | Notch depth (mm) |
|---|---|
| 20 | 1.25 |
| 20 | 2.50 |
| 20 | 3.75 |
| 30 | 3.75 |
| 40 | 3.75 |
| 50 | 3.75 |

positioned after each milling step, and the repeatability of the measurements was reduced [42].

The excitation transducer was placed 500 mm away from the center of the notch at the plate edge, and the incident wave direction was perpendicular to the normal of the notch. The transducer consisted of a PZT disc (Ferroperm Pz27, diameter 5 mm, thickness 2 mm) and a brass backing mass (diameter 5 mm, height 6 mm) and was bonded at the plate edge by a 2-component epoxy glue. Although pure excitation of the $S_0$ mode was intended, additionally the $A_0$ mode was excited with an out-of-plane amplitude a factor 3.5 lower than the $S_0$ mode amplitude, due to misalignment of the attachment of the transducer at the edge of plate. The 500 mm propagation distance between the transducer and the defect was sufficient to obtain good time separation between the incident $S_0$ and $A_0$ wave pulses.

The excitation signal was a narrowband five cycle toneburst modulated by a Hanning window with a center frequency of 100 kHz. The signal was created in a programmable function generator and amplified using a power amplifier ($200V_{pp}$). For the 5 mm plate thickness this gives a frequency-thickness product of 0.5 MHz-mm below the cut-off frequencies of the higher Lamb wave modes (approx. 1.5 MHz-mm, see Fig. 2), where only the fundamental guided wave modes ($A_0$, $S_0$, $SH_0$) exist, simplifying signal processing and consideration of mode conversion [32]. The $A_0$ mode is dispersive at low frequency-thickness products, but above 0.5 MHz-mm its group velocity is reasonably constant (around 3000 m/s) and limited pulse distortion was observed (Fig. 2). The $S_0$ mode is not very dispersive below 1 MHz-mm [21] and has the fastest group velocity (about 5400 m/s), allowing for time gating of the wave modes. In line with literature [17,19], five cycles was found to provide a good compromise between time length and frequency

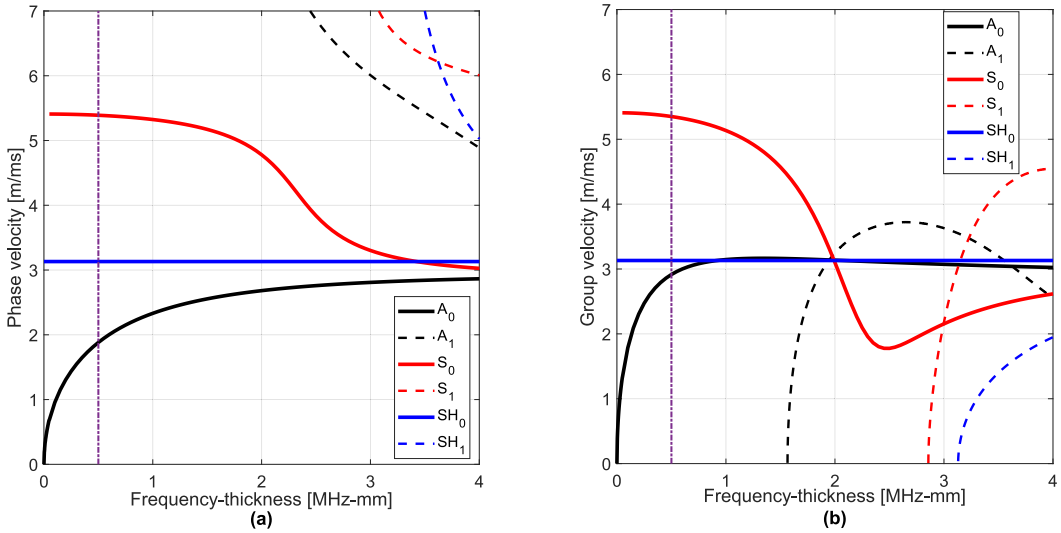


**Fig. 2.** Dispersion diagram for aluminum plate (Al 6082): (a) phase velocity; (b) group velocity; operating point at 0.5 MHz-mm frequency thickness indicated (purple, dashed-dotted line), fundamental modes (solid lines), higher order modes (dashed lines), generated using Disperse software [43].

bandwidth of the toneburst signal, limiting both signal length and pulse distortion.

For the guided wave measurements, the plate was held vertically using 4 small clamps (contact area approx. 5 mm diameter, see Fig. 1(a)) and, neglecting the contact points, can be considered as having free boundary conditions along its edges. The 0° direction was defined as the incident wave direction normal to the defect orientation, as shown in Fig. 1(b). The out-of-plane displacement velocity on the plate surface was measured using a laser vibrometer every 5° on a circle around the crack-like defect with a radius of 200 mm. At each measurement point a small retroreflective tape (approximately 5 mm x 5 mm size) was attached to improve the laser beam reflection. The measured signals (full time traces) were bandpass filtered (75–125 kHz) and averaged (20 averages) before being transferred from the digital storage oscilloscope to the data analysis PC.

Time gating was used to extract the relevant guided wave pulse from the measured time traces. The phase and amplitude (complex magnitude) at the 100 kHz center frequency were determined using FFT. A baseline measurement of the incident $S_0$ wave mode was conducted before the milling of the first notch and then a measurement of the mode-converted, scattered $A_0$ mode after each increase in defect size (milling step). Due to the limited plate size, rather tight time gating of the pulses of interest was necessary, as good time separation between the different wave pulses could not be achieved for all locations on the plate and some overlap in time occurred. Fig. 3 shows experimental time trace signals with a defect and without a defect (baseline) at two locations (0° and 60°) on the measurement circle where good and limited time separation of the wave pulses could be achieved. Baseline subtraction and time gating was applied to separate the scattered mode-converted $A_0$ mode pulse (Fig. 3(c), (d)). For some locations on the measurement circle, especially around the 60° and 330° directions, the additionally incident $A_0$ wave mode arrived at the same time as the scattered $A_0$ mode and a signal difference remained after baseline subtraction. The length of the time gating was chosen to be consistent for the evaluation of the experimental and FE results to allow like-for-like comparison. From a variation of the signal processing parameters, it was observed that the measured scattering patterns were very consistent, but that different choice of the time gating could lead to up to 5 percentage points of difference in the recorded amplitude ratios.

Additional measurements were conducted on the undamaged plate along a perpendicular line from the excitation transducer. The propagating wave pulses of the $S_0$ and $A_0$ mode were separated using time gating and the respective phase velocities [44] measured from the gradient of the phase angle with propagation distance. The experimental measurement gave values for the phase velocity of the $S_0$ and $A_0$ modes as 5464 m/s and 1896 m/s, with corresponding wavelengths of 55 mm and 19 mm.

The transducer was accidentally knocked off during the milling of the 40 mm and 50 mm length defects and reattached. The baseline data for the 40 mm and 50 mm cases has been adjusted to match the actual incidence $S_0$ mode amplitude during the measurement, but the quality of the baseline subtraction was negatively influenced. The amplitude and scattering patterns of the mode-converted $A_0$ mode could be quantified experimentally with good repeatability from the out-of-plane velocity measurement on the plate surface (laser vibrometer perpendicular to the plate surface). While the measurement of the in-plane velocity displacement (for the $S_0$ and $SH_0$ modes) is in principle possible by orienting one or multiple laser interferometers at an angle to the plate (e.g., using two laser vibrometers as reported in [23]), insufficient accuracy and repeatability was achieved in our attempts to validate the FE predictions for the $S_0$ and $SH_0$ modes.

A normalization of measured signal amplitudes relative to the strain energy density (SED) of the incident $S_0$ wave mode, measured at the notch center location before the defect was manufactured (baseline measurement), was applied. The strain energy density (per unit volume) represents the energy of each wave mode (given by the products of the stress and strain components [45]) and depends on the respective mode shapes as stated in Eq. (1).

$$SED = \frac{1}{4}\left\{\sigma_{xx}\left(\frac{\partial u_x}{\partial x}\right)+\sigma_{yy}\left(\frac{\partial u_y}{\partial y}\right)+\sigma_{zz}\left(\frac{\partial u_z}{\partial z}\right)\right\}+\frac{1}{8}\left\{\sigma_{xy}\left(\frac{\partial u_x}{\partial y}+\frac{\partial u_y}{\partial x}\right)+\sigma_{yz}\left(\frac{\partial u_y}{\partial z}+\frac{\partial u_z}{\partial y}\right)+\sigma_{xz}\left(\frac{\partial u_x}{\partial z}+\left(\frac{\partial u_z}{\partial x}\right)\right)\right\} \quad (1)$$

where $\sigma_{xx}$, $\sigma_{yy}$, and $\sigma_{zz}$ are the normal stresses, $\sigma_{xy}$, $\sigma_{yz}$ and $\sigma_{xz}$ are the shear stresses, $u_x$, $u_y$, and $u_z$ are the displacement components, and the partial derivatives of the displacement components correspond to the respective strain components.

The SED and $S_0$ and $A_0$ mode shapes through the plate thickness were

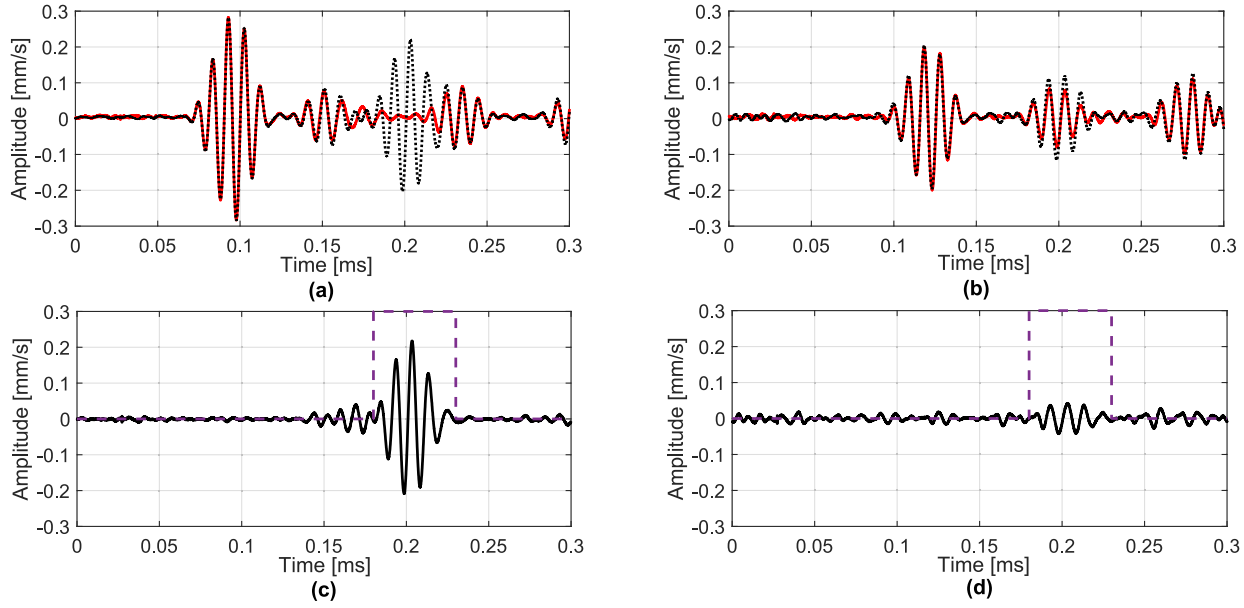


**Fig. 3.** Experimental time traces for 3.75 mm deep and 20 mm long defect measured to separate the mode-converted, scattered $A_0$ mode; signal with defect (black, dotted line) and baseline (red, solid line) at (a) 0°; (b) 60°; baseline subtraction signal (black, solid line) at (c) 0°; (d) 60°; cut-off square time window for scattered $A_0$ mode pulse: purple, dashed line.

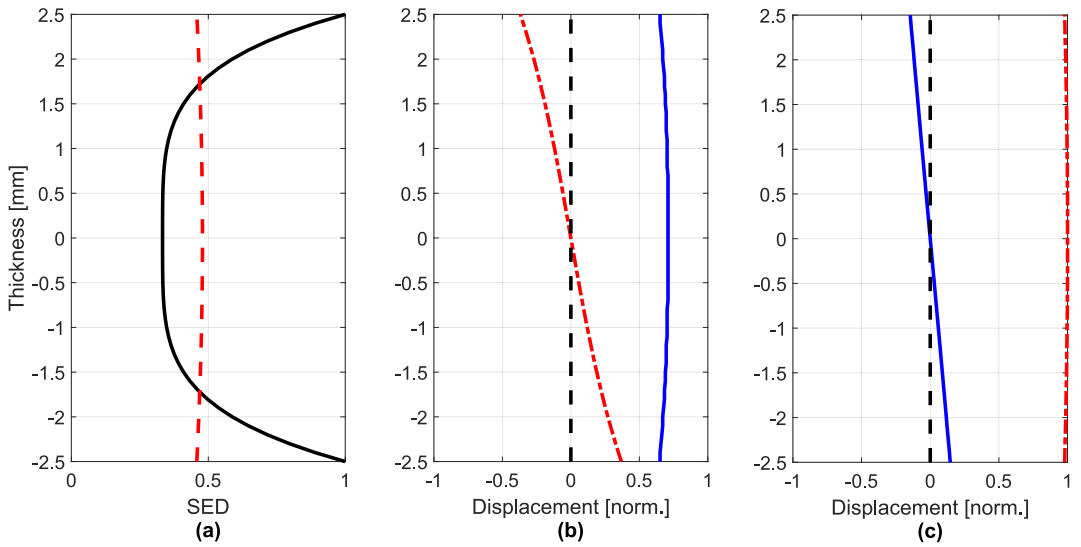


**Fig. 4.** (a) SED through thickness for $A_0$ mode (black, solid line) and $S_0$ mode (red, dashed line); (b) $A_0$ mode shape (c) $S_0$ mode shape; out-of-plane displacement: blue, solid line; in-plane displacement: red, dash-dotted line.

calculated using the Disperse software [43] and are shown in Fig. 4. The sum of the SED through the plate thickness for the $S_0$ and $A_0$ modes were calculated and the ratio of the out-of-plane displacement at the plate surface measurement to the SED obtained for both modes. For the same summed SED through the thickness, at 0.5 MHz-mm the $A_0$ mode has a factor 4.47 higher out-of-plane amplitude on the plate surface, while the $S_0$ mode has a factor 2.66 higher in-plane displacement (on the plate surface). The amplitudes of the mode-converted scattered wave modes shown in the results section were calculated using these values to represent the respective amplitude as the ratio to the SED of the incident $S_0$ wave mode.

### 2.2. Baseline-subtraction

Due to the additionally excited $A_0$ mode incident wave and top and bottom edge reflections of the incident $S_0$ mode (Fig. 5(a)), accurate time separation of the back-scattered, mode-converted $A_0$ mode was not possible for the available plate size. Fig. 5(b) shows two lobes at 60° and 330° in the polar plot of the measured $A_0$ mode-converted scattered amplitude that are due to the additionally incident $A_0$ wave mode, that arrived at the measurement points around the 60° and 330° directions at the same time as the scattered $A_0$ mode (Fig. 5(a)). The back-scattered lobe amplitude is not as smooth as the forward scattered pattern due to an overlap with the incident $S_0$ mode edge reflection. Baseline subtraction was applied to extract the pure mode-conversion and scattering (Fig. 5(c)). Baseline subtraction was applied to the FFT complex magnitude (containing both amplitude and phase information) from each measurement point, with the baseline data taken from a measurement on the undamaged plate before milling the first notch [16]. For the FE data perfect repeatability and thus baseline subtraction was possible. However, small inaccuracies in the positioning of the plate after each milling step caused slight differences in the measured amplitude and especially phase (FFT), which in turn led to a small, remaining influence when taking the complex difference in the frequency domain to the baseline measurement, as can be seen in the 60° and 330° directions in Fig. 5(c).

## 3. FE simulations

The purpose of the FE simulations was to model the guided wave scattering, understand the mode conversion and guided wave scattering patterns, and to investigate the influence of different defect parameters on detection results (sensitivity). Input files were generated by MATLAB for FE simulations using ABAQUS/Explicit [16]. The model parameters could be effectively and conveniently controlled by this process to define different defect geometries, avoiding the necessity to re-mesh in ABAQUS/CAE for changes of the defect size. Identical node numbering was applied with MATLAB, allowing full control for repeatable and accurate placement of nodal output requests [16]. The plate size was set as 1 m x 1 m × 5 mm to match the experiments. Material properties of Al 6082 aluminum alloy (Young's modulus: 73GPa, density: 2800 kg/m$^3$, Poisson's ratio: 0.33) were used to define the modeled elastic, isotropic plate. Eight-node linear brick elements with reduced integration (C3D8R, $\Delta x = \Delta y = 1$ mm, $\Delta z = 0.625$ mm) were used, as the element size should be less than 1/10th of the shortest wavelength ($A_0$ mode: 19 mm at 100 kHz) to achieve accurate FE detection results [9]. It is advantageous for the representation of through-thickness mode shapes (anti-symmetric or symmetric) to have an even number of elements through the plate thickness. It was found to be sufficient to investigate and model the part-thickness crack-like defect with eight elements ($\Delta z = 0.625$ mm) through the plate thickness (5 mm) [16]. The theoretical phase velocity of the $S_0$, $A_0$, and $SH_0$ modes at 0.5 MHz-mm were calculated using the Disperse software as 5400 m/s, 1882 m/s, and 3131 m/s, respectively, for the nominal material properties [43]. The phase velocities of the $S_0$ and $A_0$ mode were calculated as 5333 m/s and 1905 m/s from the FE simulations and as 5464 m/s and 1896 m/s from additional experimental measurements, with acceptable percentage errors of up to 1.2 %. The theoretically calculated wavelengths of the $S_0$, $A_0$, and $SH_0$ modes at 100 kHz are 54 mm, 19 mm, and 31 mm, respectively.

The mode conversion and scattering from an incident $S_0$ wave mode pulse to the $A_0$, $SH_0$, and $S_0$ wave modes was simulated and evaluated. An in-plane point force excitation was applied at an edge node (500 mm from the defect location) to achieve limited (ideally plane) incident wave front curvature. An additional out-of-plane point force was excited at the same location to simulate the (unwanted) additionally excited $A_0$ mode observed in the experiments. To obtain and match the experimentally measured factor of 3.5 ($S_0/A_0$ out-of-plane amplitude on plate surface), the out-of-plane point force magnitude was set as 0.013 of the in-plane force magnitude. The center frequency was set at 100 kHz with five cycles of a narrowband pulse (sinusoid in a Hanning window), matching the experiments. A frequency thickness product of 0.5 MHz-mm was chosen, with limited $A_0$ and $S_0$ mode pulse distortion. The excitation signal amplitude, $x(t)$ is given by

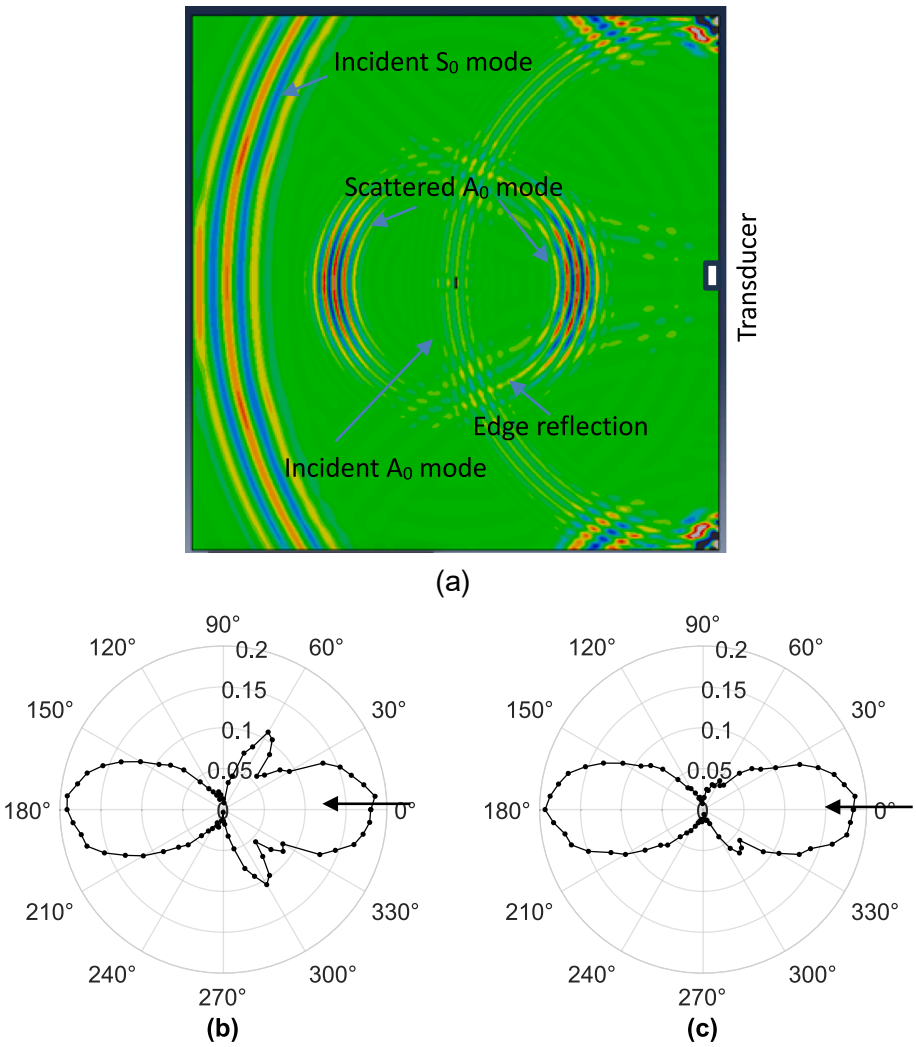


**Fig. 5.** Baseline subtraction for amplitude of scattered $A_0$ mode at 20 mm long and 3.75 mm deep defect: (a) snapshot of FE simulation out-of-plane displacement at surface; experimental amplitude polar plot (b) without baseline subtraction; (c) with baseline subtraction (arrow: incident wave direction).

$$x(t) = 0.5(1 - cos(\frac{2\pi ft}{N}))sin(2\pi ft) \quad (2)$$

where $t$ is time, $f$ is the center frequency, and $N$ is the number of the cycles.

The crack-like defect (perpendicular to the incident wave propagation direction) was located at the plate center and the point excitation was located at the plate edge to match the experimental configuration. The depth (0 to 5 mm) and length (0 to 100 mm) of the defect was changed. One row of the brick elements was removed to model the crack-like defect as a notch, without changing the Cartesian mesh at other locations of the plate, keeping the monitoring points for the baseline subtraction identical (Fig. 6). Previous studies had found that mesh refinement around the defect was not required for sufficiently small mesh size [9,16]. The notch width was set to 1 mm with right-angle corners, reasonably matching the geometry of the milled notch in the experiments. A notch rather than a fatigue crack (zero width) was studied as it is easier to manufacture for the experimental validation. No significant difference is expected as the wavelength is significantly longer than the notch width. Explicit time integration with a time step of 0.02 μs and a total simulation time of 0.3 ms was applied. The time step was chosen small enough to avoid stability problems [9]. Free boundary conditions were used for the plate to match the experiments, where the plate was only held in four points at the plate top and bottom edge as shown in Fig. 1(a).

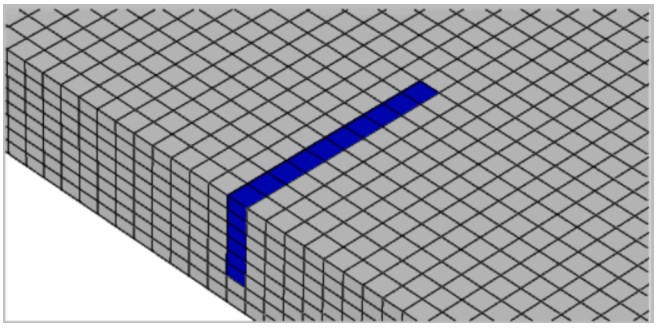

**Fig. 6.** Schematic (cut through plate thickness) showing Cartesian mesh around 10 mm long and 3.75 mm deep notch, removing six rows of elements through thickness (blue); C3D8R element type size ($\Delta x = \Delta y = 1$ mm, $\Delta z = 0.625$ mm).

To match the experimental configuration, a monitoring circle with 200 mm radius around the notch was defined with monitoring points every 5° (totally 72 points), interpolated from the Cartesian mesh points on the plate surface, and the out-of-plane displacement was recorded. For each monitoring point, the time history output data was extracted from ABAQUS and saved in MATLAB format for analysis. For the displacement data at each monitoring point, FFT was used to obtain the complex magnitude (phase angle and amplitude) at the center frequency

(100 kHz) [37]. Baseline subtraction was applied to the FFT complex magnitude relative to the simulation results for an undamaged plate. For the scattered $S_0$ and $SH_0$ modes, the two in-plane displacement components were recorded at the half-thickness location. Time gating was used to separate the $S_0$ and $SH_0$ mode wave pulses (respective group velocities: 5400 m/s and 3131 m/s). For the $S_0$ and $SH_0$ modes, both modes have two in-plane displacement components, and the respective amplitudes were combined by the square root of the sum of the square of the components to give respectively the tangential and radial displacement of the $S_0$ and $SH_0$ modes. To make the data comparable, the normalized amplitude of the scattered $A_0$ or $SH_0$ mode was multiplied with a normalization ratio to obtain the same sum of the strain energy density (SED) through the thickness as the $S_0$ mode, as stated in the experimental section above.

## 4. Mode conversion and scattering at part-thickness defect

The influence of defect depth and length on the $S_0$ mode scattering and $A_0$ and $SH_0$ mode conversion were investigated from FE simulations and validated from the experiments for the $A_0$ mode. The scattering patterns of the $A_0$, $S_0$, and $SH_0$ modes at the defect were investigated for different defect parameters. Amplitudes are shown normalized to the SED of the incident $S_0$ Lamb wave mode at the defect center without defect (baseline).

### 4.1. Influence of defect depth

For the perpendicular incident $S_0$ mode, the forward and backward scattering patterns of the mode-converted $A_0$ and $S_0$ mode are perpendicular relative to the defect orientation (Figs. 7 and 8). The backward lobe is the energy reflected at the defect towards the excitation location (0° direction). For the $S_0$ mode the forward lobe (180° direction) indicates a reduction of the amplitude of the $S_0$ mode propagating past the defect. For the $SH_0$ mode, no mode conversion of the perpendicular incident $S_0$ mode occurs along the length of the defect and the scattering patterns with 4 lobes in the diagonal directions (approximately 45°, 135°, 225°, and 315°) are driven by the mode conversion at the defect corners (Fig. 9).

In order to validate the FE predictions, simulation and experimental results for the mode version to the $A_0$ mode were compared for six cases (20 mm long notch with three different depths and 3.75 mm deep notch with three different lengths). For each case, the ratio (percentage) of the summed square of the difference in normalized amplitude between simulation and experimental results for each measurement point (every 5°) to the summed squared simulation amplitude was calculated to quantify the agreement [16]. This includes contributions from experimental noise as well as systematic differences, e.g., scattering lobes at different angles or amplitudes. For the incident $S_0$ mode perpendicular to the 20 mm long notch (0° incidence angle), generally good agreement of the angular amplitude patterns between FE simulations and experimental results was obtained, as shown in Fig. 7 for all notch depths (1/4, 1/2, 3/4). The respective percentage differences for the three depths (shallow to deep) are 5 %, 1.2 %, and 0.4 %. The experimental measurement errors change for each case, but in general the agreement improves with increasing defect depth as the scattered amplitude increases. Similar agreement was previously obtained for the scattering of the $A_0$ Lamb wave mode at part-thickness crack-like defects ($A_0$-$A_0$ mode) [16].

For the FE simulations, the forward and backward patterns of the scattered $A_0$ mode have similar amplitude with a maximum percentage difference of 10 % for the 1.25 mm deep defect (Fig. 7(a)). For the experimental results, the forward scattered patterns look smoother than the backward scattered patterns because of the overlap in time with the incident $A_0$ mode and the edge reflection necessitating baseline

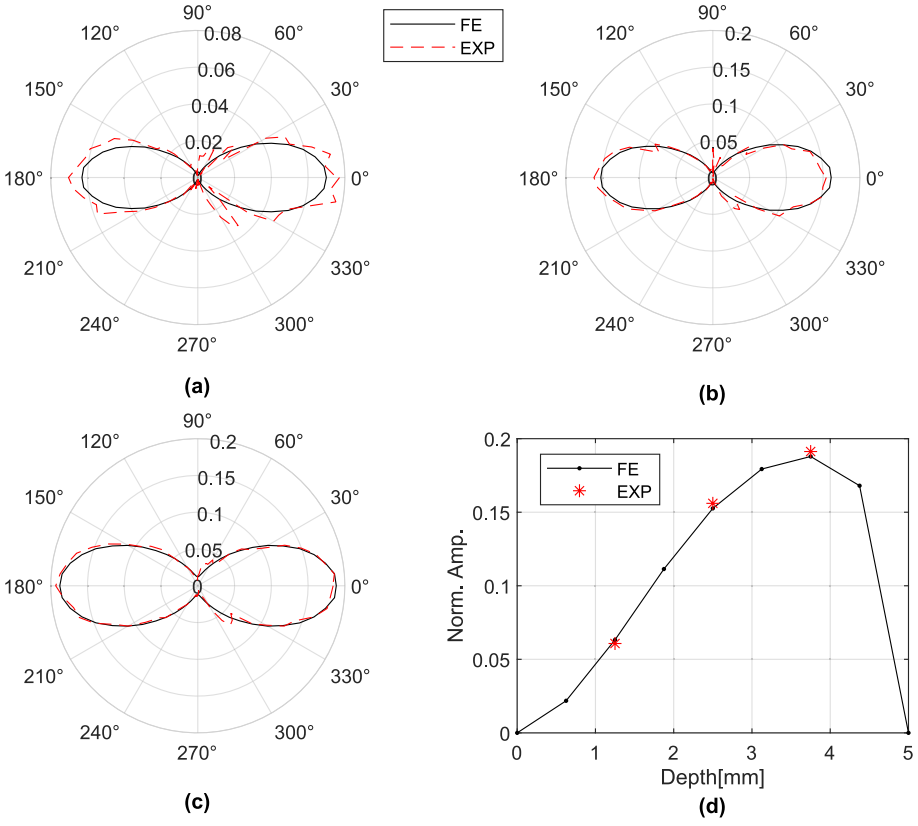


**Fig. 7.** Polar plots of normalized amplitude of $A_0$ mode scattered at 20 mm long notch: (a) 1.25 mm depth; (b) 2.5 mm depth; (c) 3.75 mm depth; (d) normalized $A_0$ mode amplitude for variation of depth. FE simulations: black solid line and dots; experiment: red dashed line and stars.

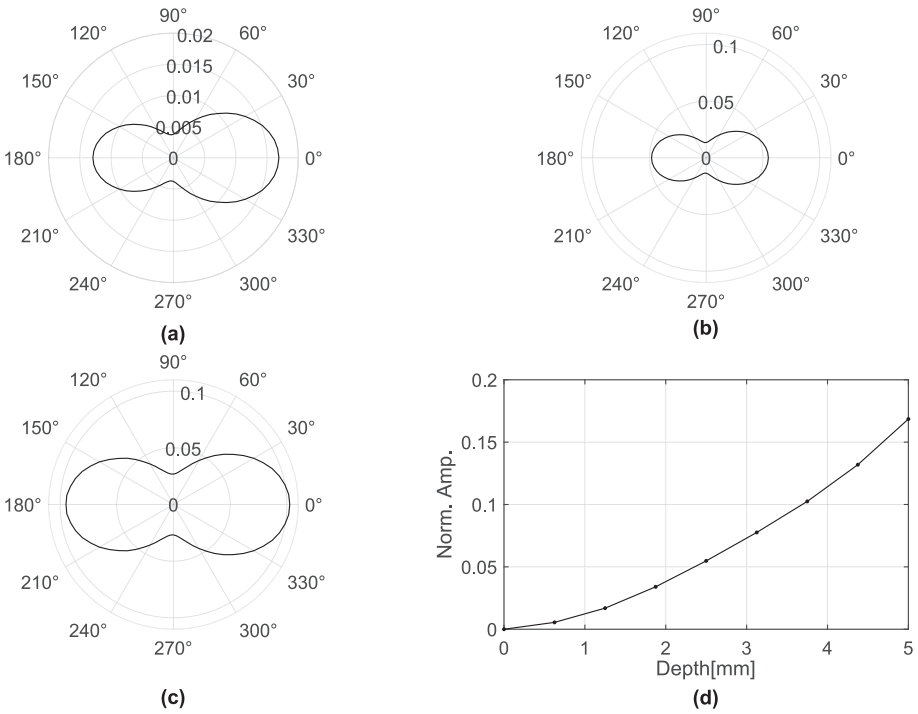


**Fig. 8.** Polar plots of normalized amplitude of $S_0$ mode scattered at 20 mm long notch: (a) 1.25 mm depth; (b) 2.5 mm depth; (c) 3.75 mm depth; (d) normalized amplitude of $S_0$ mode scattered at defect for variation of depth. FE simulations: black solid line and dots.

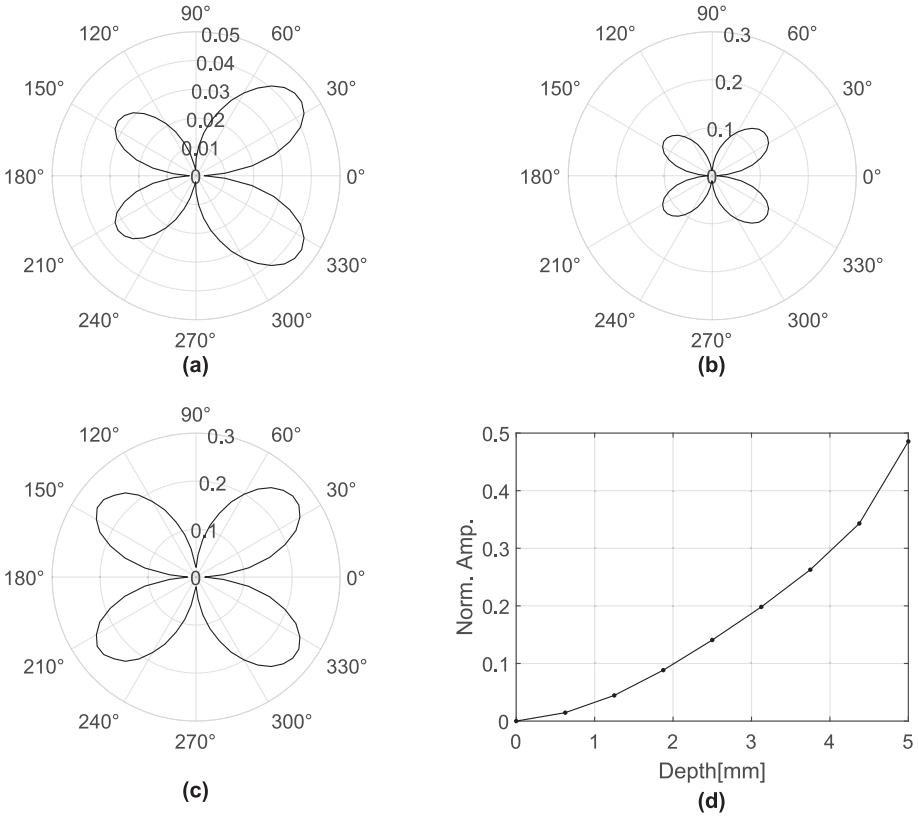


**Fig. 9.** Polar plots of normalized amplitude of $SH_0$ mode scattered at 20 mm long notch: (a) 1.25 mm depth; (b) 2.5 mm depth; (c) 3.75 mm depth; (d) normalized amplitude of $SH_0$ mode scattered at defect for variation of depth. FE simulations: black solid line and dots.

subtraction. For the scattered $S_0$ and $SH_0$ modes, the backward scattering has higher amplitude than the forward scattering at the shallow defect (Fig. 8(a), Fig. 9(a)). In general, the scattering patterns for all three modes remain similar for different defect depths, but the amplitude changes. In Fig. 7(d), the scattered $A_0$ mode amplitude for different defect depths is plotted. Increased scattering occurs as the defect

becomes more severe (deeper), but mode conversion must also be considered. No mode conversion occurs for the through-thickness defect, as indicated by the zero amplitude. Most mode conversion is expected to theoretically occur at half thickness (2.5 mm) defect depth. The maximum $A_0$ mode amplitude occurs at approximately 3/4 (3.75 mm) defect depth due to the combination of the two effects. Similar behaviour was previously predicted from FE simulations at a comparable frequency-thickness product (0.6 MHz-mm), with the highest amplitude of the mode-converted $A_0$ mode amplitude obtained for a 2/3-thickness defect depth [41]. In Fig. 8(d) and Fig. 9(d), it can be seen that the scattered $S_0$ and $SH_0$ mode amplitude increases as the defect depth increases and the maximum magnitude occurs for the through-thickness defect. For the considered defect length of 20 mm (comparable to the $A_0$ and $SH_0$ wavelengths, but much shorter than the $S_0$ wavelength), the $SH_0$ mode has the highest normalized amplitude of the three modes for deep defects (depth larger than half-thickness). For shallow defects (depth less than half-thickness) the mode-converted scattered $A_0$ mode had the highest amplitude and the $S_0$ mode had the lowest amplitude, similar to previous FE simulation predictions [41].

### 4.2. Influence of defect length

For the 3.75 mm deep notch, generally good agreement of the angular amplitude patterns between FE predictions and experimental results can be seen in Fig. 10 for the mode converted $A_0$ mode at different notch lengths (30 mm, 40 mm, and 50 mm). The percentage differences for three lengths (short to long) are 1.6 %, 3.5 %, and 3 %. Due to the transducer being knocked off and reattached for the 40 mm and 50 mm length measurements, the agreement is not as good as there are slight differences compared to the baseline data. Again, the forward and backward patterns of the scattered $A_0$ mode have almost the same forward and backward scattered amplitude with a maximum percentage difference of 1.5 % for the 50 mm long crack. As shown in Fig. 10(d), the sensitivity (amplitude) of the mode converted $A_0$ mode increases almost linearly as the defect length increases from 0 mm to 80 mm. For short defect lengths between 0 and 20 mm some variability is predicted and above 90 mm, the slope drops. Fig. 10 indicates that the normalized amplitude of the mode-converted wave ($S_0$ to $A_0$ mode) could potentially be used to predict the defect length for a given defect depth and incident wave angle (perpendicular).

For the scattered $S_0$ mode, the polar plot patterns change somewhat as the defect length increases, with the perpendicular scattered amplitude (0° and 180°) becoming more prominent as the defect length increases from 30 mm (Fig. 11(a)) to 50 mm (Fig. 11(c), comparable to the $S_0$ wavelength). The $S_0$ mode polar patterns for the 50 mm long defect are very similar to the $A_0$ mode polar patterns for 20 mm length (Fig. 7(c)) as the defect length/wavelength ratio is similar. The normalized amplitude of the $S_0$ mode increases almost linearly as the defect length increases from 0 to 100 mm without the slope dropping off for long defects (Fig. 11(d)). However, the normalized amplitude of the $S_0$ mode is lower than the normalized amplitude of the $A_0$ mode for the same part-thickness defect size, e.g., 0.1 compared to 0.2 for 20 mm length. The $A_0/S_0$ mode amplitude ratio is almost constant at 1.9 for defect lengths between 10 mm and 80 mm as more energy is transferred into the $A_0$ mode having a shorter wavelength. Similar polar plot patterns compared with previous FE simulations [41] were obtained, as the defect length is comparable to the $S_0$ mode wavelength and two lobes symmetric to the defect orientation can be observed (Fig. 11).

For the $SH_0$ mode, the polar patterns change as the defect length increases due to the interference of the mode-conversion and scattering at the two notch tips (Fig. 12). For the perpendicular incident $S_0$ mode no mode conversion to the $SH_0$ mode occurs along the length of the notch, but only at the corners. This generated $SH_0$ mode pulses that radiated at an angle, originating at the defect corners, and the observed amplitude distribution can be considered as an overlap of two circular scattering patterns [23]. The direction of the four large lobes at approximately 45°, 135°, 225°, and 315° for 20 mm length gradually changes to 20°, 140°, 200°, and 340° direction for the 50 mm long defect

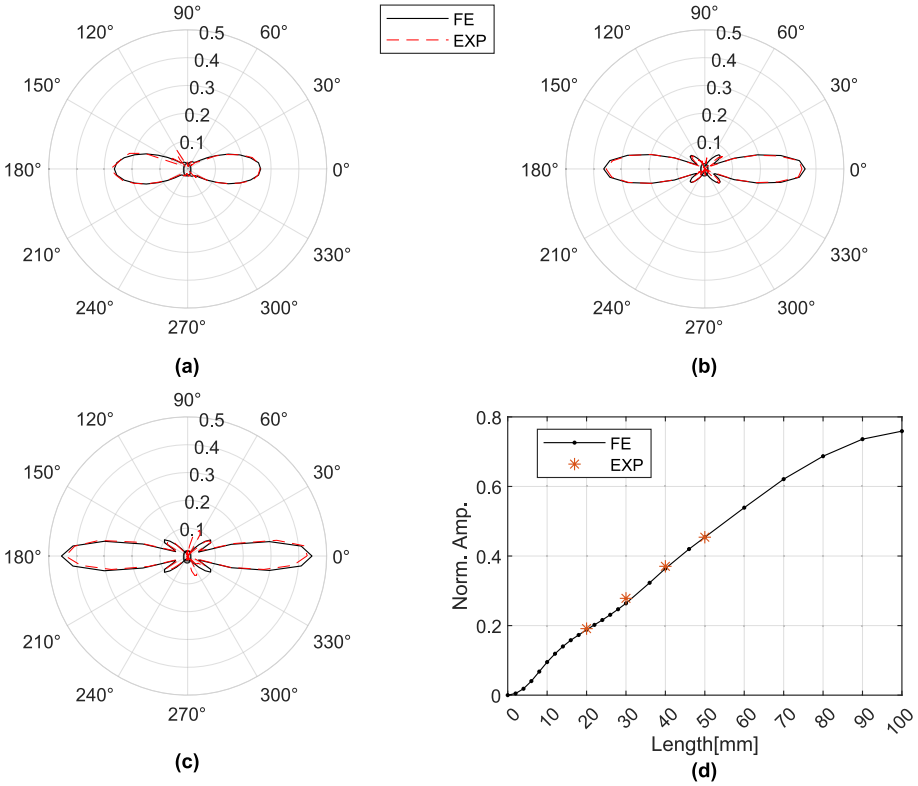


**Fig. 10.** Polar plots of normalized amplitude of $A_0$ mode scattered at 3.75 mm deep notch: (a) 30 mm length; (b) 40 mm length; (c) 50 mm length; (d) normalized $A_0$ mode amplitude for variation of length. FE simulations: black solid line and dots; experiment: red dashed line and stars.

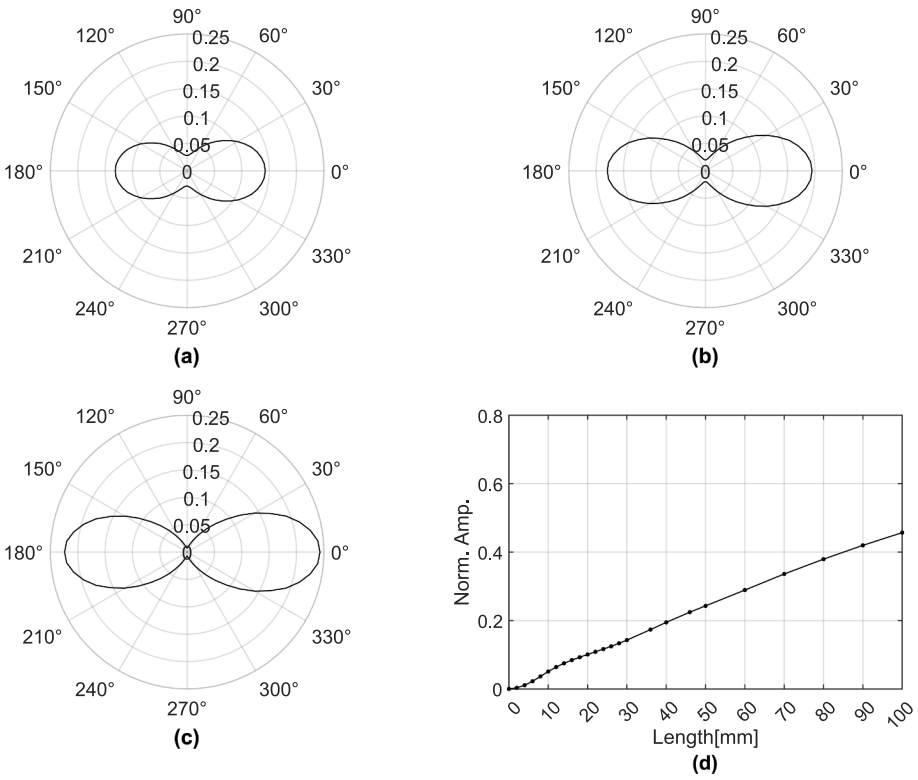


**Fig. 11.** Polar plots of normalized amplitude of $S_0$ mode scattered at 3.75 mm deep notch: (a) 30 mm length; (b) 40 mm length; (c) 50 mm length; (d) normalized $S_0$ mode amplitude for variation of length. FE simulations: black solid line and dots.

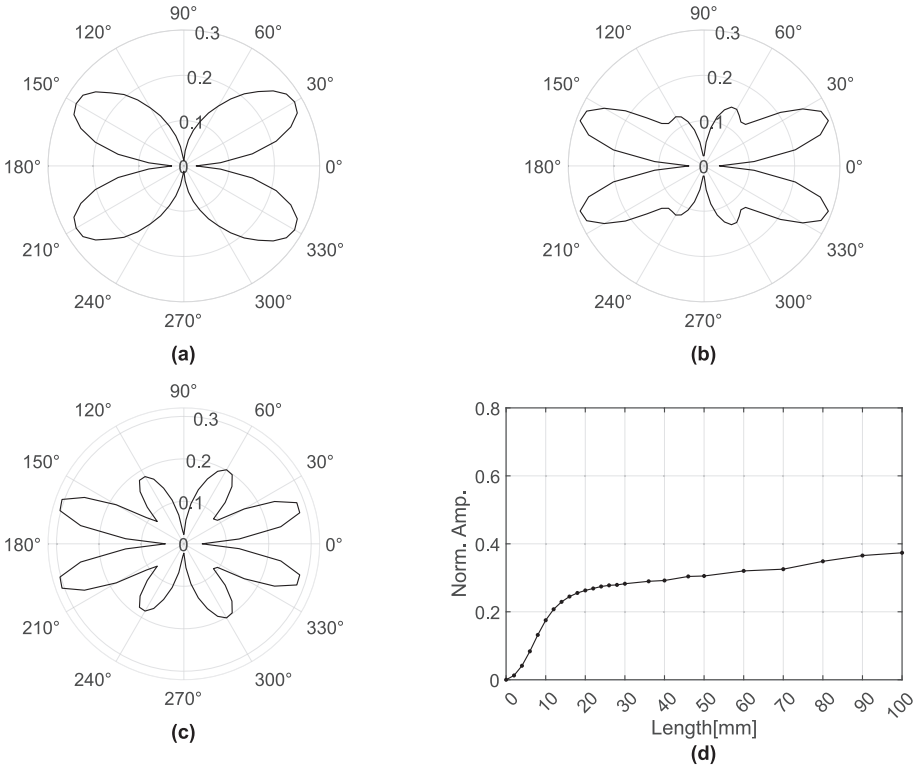


**Fig. 12.** Polar plots of normalized amplitude of $SH_0$ mode scattered at 3.75 mm deep notch: (a) 30 mm length; (b) 40 mm length; (c) 50 mm length; (d) normalized $SH_0$ mode amplitude for variation of length. FE simulations: black solid line and dots.

and four additional small lobes at 60°, 120°, 240°, and 300° are generated (Fig. 12(c)). For short defects (20 mm length, comparable to the $SH_0$ wavelength) the respective scattered pulses at the two defect ends overlapped and gave the quadrupole patterns seen in Fig. 9 and Fig. 12(a). For longer defects the interaction of the corner scattered wave pulses is more complex and resulted in the observed octupole patterns observed for the geometries shown in Fig. 12. Previous FE simulations [41] for a partial, 1/3-thickness defect also showed four large lobes, similar to this study.

The normalized amplitude of the $SH_0$ mode does not increase linearly with the defect length as the $A_0$ and $S_0$ modes, and it only slightly increases for defect lengths above 20 mm. The mode conversion of the $S_0$ to the $SH_0$ mode does not occur along the defect length for perpendicular incidence, but only occurs at the corner of the defect, which explains why the normalized amplitude does not significantly increase with the defect length. The amplitude of $SH_0$ mode is the highest among three modes for short, deep defects but for defect lengths above 40 mm, the $A_0$ mode has the highest amplitude. The $S_0$ mode amplitude is higher than the $SH_0$ mode amplitude once the defect length is beyond 70 mm. Previous FE simulations concluded that the defect depth influenced the distribution of the energy transferred into each wave mode, but defect lengths beyond the $S_0$ mode wavelength were not investigated [41].

## 5. Conclusions

Early and efficient detection of part-thickness fatigue cracks is important, as fatigue causes a large percentage of failures in metallic aircraft components. Guided ultrasonic waves can propagate significant distances along large, thin structures. For part-thickness defects in plates, it is important to fully understand the scattering and mode conversion of low frequency guided waves to improve the nondestructive testing and health monitoring of such large structures. The mode-converted scattering of the perpendicularly incident $S_0$ mode to the $A_0$ mode at part-thickness crack-like defects in an aluminum plate was investigated from FE simulations and experimentally validated. Good agreement of the polar scattering patterns and normalized amplitude between FE simulations and experiments was obtained with percentage differences of less than 5 %. The scattered $S_0$ and mode-converted $SH_0$ mode at the defect were studied from FE simulations. The influence of defect depth and length on detection results was investigated. For perpendicular incidence, the forward and backward scattering patterns of the mode-converted $A_0$ and $S_0$ modes are perpendicular to the defect orientation. For the scattered $A_0$ mode, the forward and backward patterns have very similar amplitude, independent of the defect size. The highest sensitivity for the $A_0$ mode occurs at the 3/4 defect depth and the normalized amplitude increases almost linearly with defect length, with the slope dropping only for very long defects. The $A_0$ mode has the highest normalized amplitude for long defects. For the $S_0$ mode, the backward scattering is larger than the forward scattering at shallow defects. The normalized amplitude increases as the defect depth and length increase. The polar plot patterns change as the defect length changes and become similar to the $A_0$ mode patterns when the defect length/wavelength ratio is similar. For the $SH_0$ mode, more complex scattering patterns with lobes in different directions were predicted for short defects. As the mode conversion to the $SH_0$ mode occurs at the defect corners for perpendicular incidence, the lobe direction and patterns change with defect length. The $SH_0$ mode has the highest amplitude for short defects but the normalized amplitude does not significantly increase with increasing defect length. Better understanding and comparison of the scattering and mode conversion of the low-frequency, fundamental guided wave modes were obtained. These findings could potentially be employed to improve the sensitivity of SHM by incorporating the information contained in the mode-converted guided wave modes in localization and detection algorithms.

## CRediT authorship contribution statement

**Lijian Li:** Writing – original draft, Validation, Methodology, Investigation, Formal analysis. **Paul Fromme:** Writing – review & editing, Supervision, Software, Methodology, Investigation, Conceptualization.

## Declaration of competing interest

The authors declare that they have no known competing financial interests or personal relationships that could have appeared to influence the work reported in this paper.

## Data availability

Data will be made available on request.

## References

[1] S.K. Bhaumik, M. Sujata, M.A. Venkataswamy, Fatigue failure of aircraft components, Eng. Fail. Anal. 15 (6) (2008) 675–694, https://doi.org/10.1016/j.engfailanal.2007.10.001.
[2] Z. Marusic, D. Bartulovic, B. Makovic, Methods to detect and prevent fatigue in aging aircraft structures, Tehnicki Vjesnik-Technical Gazette 22 (3) (2015) 793–803, https://doi.org/10.17559/tv-20140702111704.
[3] J.M. Papazian, J. Nardiello, R.P. Silberstein, G. Welsh, D. Grundy, C. Craven, L. Evans, N. Goldfine, J.E. Michaels, T.E. Michaels, Y.F. Li, C. Laird, Sensors for monitoring early stage fatigue cracking, Int. J. Fatigue 29 (9–11) (2007) 1668–1680, https://doi.org/10.1016/j.ijfatigue.2007.01.023.
[4] J. Mishael, P.G. Morato, P. Rigo, Numerical fatigue modeling and simulation of interacting surface cracks in offshore wind structural connections, Mar. Struct. 92 (2023) 103472, https://doi.org/10.1016/j.marstruc.2023.103472.
[5] J.S. Hall, J.E. Michaels, Multipath ultrasonic guided wave imaging in complex structures, Struct. Health Monit. 14 (4) (2015) 345–358, https://doi.org/10.1177/1475921715578316.
[6] Rose, J. L. (2014). *Ultrasonic Guided Waves in Solid Media*. (Cambridge University Press). doi:10.1017/cbo9781107273610.
[7] M. Mitra, S. Gopalakrishnan, Guided wave based structural health monitoring: a review, Smart Mater. Struct. 25 (5) (2016) 053001, https://doi.org/10.1088/0964-1726/25/5/053001.
[8] C.H. Wang, J.T. Rose, F.K. Chang, A synthetic time-reversal imaging method for structural health monitoring, Smart Mater. Struct. 13 (2) (2004) 415–423, https://doi.org/10.1088/0964-1726/13/2/020.
[9] P.S. Tua, S.T. Quek, Q. Wang, Detection of cracks in plates using piezo-actuated Lamb waves, Smart Mater. Struct. 13 (4) (2004) 643–660, https://doi.org/10.1088/0964-1726/13/4/002.
[10] P.S. Tua, S.T. Quek, Q. Wang, Detection of cracks in cylindrical pipes and plates using piezo-actuated Lamb waves, Smart Mater. Struct. 14 (6) (2005) 1325–1342, https://doi.org/10.1088/0964-1726/14/6/025.
[11] V.A. Attarian, F.B. Cegla, P. Cawley, Long-term stability of guided wave structural health monitoring using distributed adhesively bonded piezoelectric transducers, Struct. Health Monit. 13 (3) (2014) 265–280, https://doi.org/10.1177/1475921714522842.
[12] G. Konstantinidis, B.W. Drinkwater, P.D. Wilcox, The temperature stability of guided wave structural health monitoring systems, Smart Mater. Struct. 15 (4) (2006) 967–976, https://doi.org/10.1088/0964-1726/15/4/010.
[13] H.L. Li, J.E. Michaels, S.J. Lee, T.E. Michaels, Quantification of surface wetting in plate-like structures via guided waves, AIP Conf. Proc. 1430 (2011) 217–224, https://doi.org/10.1063/1.4716233.
[14] J.E. Michaels, T.E. Michaels, Guided wave signal processing and image fusion for in situ damage localization in plates, Wave Motion 44 (6) (2007) 482–492, https://doi.org/10.1016/j.wavemoti.2007.02.008.
[15] J.E. Michaels, Detection, localization and characterization of damage in plates with an in situ array of spatially distributed ultrasonic sensors, Smart Mater. Struct. 17 (3) (2008) 035035, https://doi.org/10.1088/0964-1726/17/3/035035.
[16] P. Fromme, Guided wave sensitivity prediction for part and through-thickness crack-like defects, Struct. Health Monit. 19 (3) (2020) 953–963, https://doi.org/10.1177/1475921719892205.
[17] M.J.S. Lowe, O. Diligent, Low-frequency reflection characteristics of the s(0) Lamb wave from a rectangular notch in a plate, J. Acoust. Soc. Am. 111 (1) (2002) 64–74, https://doi.org/10.1121/1.1424866.
[18] M.J.S. Lowe, P. Cawley, J.Y. Kao, O. Diligent, The low frequency reflection characteristics of the fundamental antisymmetric Lamb wave a(0) from a rectangular notch in a plate, J. Acoust. Soc. Am. 112 (6) (2002) 2612–2622, https://doi.org/10.1121/1.1512702.
[19] A. Demma, P. Cawley, M. Lowe, Scattering of the fundamental shear horizontal mode from steps and notches in plates, J. Acoust. Soc. Am. 113 (4) (2003) 1880–1891, https://doi.org/10.1121/1.1554694.
[20] Y. Alkassar, V.K. Agarwal, E. Alshrihi, Simulation of Lamb wave modes conversions in a thin plate for damage detection, Procedia Eng. 173 (2017) 948–955, https://doi.org/10.1016/j.proeng.2016.12.153.

[21] Y. Lu, L. Ye, Z.Q. Su, C.H. Yang, Quantitative assessment of through-thickness crack size based on Lamb wave scattering in aluminium plates, NDT and E Int. 41 (1) (2008) 59–68, https://doi.org/10.1016/j.ndteint.2007.07.003.
[22] R. Soleimanpour, C.-T. Ng, Scattering of the fundamental anti-symmetric Lamb wave at through-thickness notches in isotropic plates, J. Civ. Struct. Heal. Monit. 6 (3) (2016) 447–459, https://doi.org/10.1007/s13349-016-0166-7.
[23] P. Rajagopal, M.J.S. Lowe, Short range scattering of the fundamental shear horizontal guided wave mode normally incident at a through-thickness crack in an isotropic plate, J. Acoust. Soc. Am. 122 (3) (2007) 1527–1538, https://doi.org/10.1121/1.2764472.
[24] P. Rajagopal, M.J.S. Lowe, Angular influence on the scattering of fundamental shear horizontal guided waves by a through-thickness crack in an isotropic plate, J. Acoust. Soc. Am. 124 (4) (2008) 2021–2030, https://doi.org/10.1121/1.2968697.
[25] P. Rajagopal, M.J.S. Lowe, Scattering of the fundamental shear horizontal guided wave by a part-thickness crack in an isotropic plate, J. Acoust. Soc. Am. 124 (5) (2008) 2895–2904, https://doi.org/10.1121/1.2982410.
[26] X. Chen, J.E. Michaels, T.E. Michaels, A methodology for estimating guided wave scattering patterns from sparse transducer array measurements, IEEE Trans. Ultrason. Ferroelectr. Freq. Control 62 (1) (2015) 208–219, https://doi.org/10.1109/tuffc.2014.006747.
[27] H.Y. Liu, X. Chen, J.E. Michaels, T.E. Michaels, C.F. He, Incremental scattering of the A(0) Lamb wave mode from a notch emanating from a through-hole, Ultrasonics 91 (2019) 220–230, https://doi.org/10.1016/j.ultras.2018.08.004.
[28] N. Quaegebeur, N. Bouslama, M. Bilodeau, R. Guitel, P. Masson, A. Maslouhi, P. Micheau, Guided wave scattering by geometrical change or damage: application to characterization of fatigue crack and machined notch, Ultrasonics 73 (2017) 187–195, https://doi.org/10.1016/j.ultras.2016.09.014.
[29] H.J. Cho, C.J. Lissenden, Structural health monitoring of fatigue crack growth in plate structures with ultrasonic guided waves, Struct. Health Monit. 11 (4) (2012) 393–404, https://doi.org/10.1177/1475921711430439.
[30] K. Cho, Estimation of ultrasonic guided wave mode conversion in a plate with thickness variation, IEEE Trans. Ultrason. Ferroelectr. Freq. Control 47 (3) (2000) 591–603, https://doi.org/10.1109/58.842046.
[31] N. Terrien, D. Osmont, D. Royer, F. Lepoutre, A. Déom, A combined finite element and modal decomposition method to study the interaction of Lamb modes with micro-defects, Ultrasonics 46 (1) (2007) 74–88, https://doi.org/10.1016/j.ultras.2006.11.001.
[32] O. Diligent, T. Grahn, A. Boström, P. Cawley, M.J.S. Lowe, The low-frequency reflection and scattering of the S0 Lamb mode from a circular through-thickness hole in a plate: finite element, analytical and experimental studies, J. Acoust. Soc. Am. 112 (6) (2002) 2589–2601, https://doi.org/10.1121/1.1512292.
[33] F. Benmeddour, S. Grondel, J. Assaad, E. Moulin, Study of the fundamental Lamb modes interaction with asymmetrical discontinuities, NDT and E Int. 41 (5) (2008) 330–340, https://doi.org/10.1016/j.ndteint.2008.01.004.
[34] N. Mori, S. Biwa, T. Kusaka, Damage localization method for plates based on the time reversal of the mode-converted Lamb waves, Ultrasonics 91 (2019) 19–29, https://doi.org/10.1016/j.ultras.2018.07.007.
[35] P. Aryan, A. Kotousov, C.T. Ng, B.S. Cazzolato, A baseline-free and non-contact method for detection and imaging of structural damage using 3D laser vibrometry, Struct. Control Health Monit. 24 (4) (2017) e1894, doi:10.1002/stc.1894.
[36] L. Zhou, Z.Q. He, H. Sun, Lamb wave mode conversion-based crack detection for plate-like structures without baseline information, J. Vibroeng. 15 (2) (2013) 647–657. ISSN: 1392–8716.
[37] A. Ghadami, M. Behzad, H.R. Mirdamadi, A mode conversion-based algorithm for detecting rectangular notch parameters in plates using Lamb waves, Arch. Appl. Mech. 85 (6) (2015) 793–804, https://doi.org/10.1007/s00419-015-0991-x.
[38] H.B. Jia, H.W. Liu, Z.C. Zhang, F.H. Dai, Y.J. Liu, J.S. Leng, A baseline-free approach of locating defect based on mode conversion and the reciprocity principle of Lamb waves, Ultrasonics 102 (2020) 106063, https://doi.org/10.1016/j.ultras.2020.106063.
[39] K.L. Xu, D. Ta, Z.Q. Su, W.Q. Wang, Transmission analysis of ultrasonic Lamb mode conversion in a plate with partial-thickness notch, Ultrasonics 54 (1) (2014) 395–401, https://doi.org/10.1016/j.ultras.2013.07.011.
[40] F.B. Cegla, A. Rohde, M. Veidt, Analytical prediction and experimental measurement for mode conversion and scattering of plate waves at non-symmetric circular blind holes in isotropic plates, Wave Motion 45 (3) (2008) 162–177, https://doi.org/10.1016/j.wavemoti.2007.05.005.
[41] Y. Zheng, J. Zhou, Mode conversion and scattering properties of Lamb waves near localized cracking, Eng. Mech. 31 (6) (2014) 21–29, https://doi.org/10.6052/j.issn.1000-4750.2012.12.0982.
[42] L. Li, P. Fromme, Experimental validation of guided wave mode conversion at part thickness defects in metal plate, Proceedings SPIE 12951 (2024) 1295116, https://doi.org/10.1117/12.3012582.
[43] Pavlakovic, B., Lowe, M., Alleyne, D., Cawley, P. (1997). Disperse: A general purpose program for creating dispersion curves. In: Thompson, D.O., Chimenti, D. E. (eds) Review of Progress in Quantitative Nondestructive Evaluation, 16, 185-192. doi:10.1007/978-1-4615-5947-4_24.
[44] W. Sachse, Y.-H. Pao, On the determination of phase and group velocities of dispersive waves in solids, J. Appl. Phys. 49 (8) (1978) 4320–4327, https://doi.org/10.1063/1.325484.
[45] Auld, B. A. (1990). Acoustic fields and waves in solids, Volume 2. 2nd Edition, Krieger Publishing Company, Malabar.